Mon. Not. R. Astron. Soc. **393,** 1433–1448 (2009) doi:10.1111/j.1365-2966.2008.14171.x

Gravitationally distorted P Cygni profiles from outflows near compact objects

A. V. Dorodnitsyn[1,2]★

[1] *Laboratory for High Energy Astrophysics, NASA Goddard Space Flight Center, Code 662, Greenbelt, MD 20771, USA*
[2] *Space Research Institute, Profsoyuznaya st., 84/32, 117997 Moscow, Russia*

Accepted 2008 October 29. Received 2008 October 6; in original form 2006 September 8

ABSTRACT

We consider resonant absorption in a spectral line in the outflowing plasma within several tens of Schwarzschild radii from a compact object. We take into account both Doppler and gravitational shifting effects and reformulate the theory of P Cygni profiles in these new circumstances. It is found that a spectral line may have multiple absorption and emission components depending on how far the region of interaction is from the compact object and what the distribution of velocity and opacity is. Profiles of spectral lines produced near a neutron star or a black hole can be strongly distorted by Doppler blue- or redshifting and gravitational redshifting. These profiles may have both red- and blueshifted absorption troughs. The result should be contrasted with classical P Cygni profiles, which consist of redshifted emission and blueshifted absorption features.

We suggest that this property of line profiles to have complicated narrow absorption and emission components in the presence of strong gravity may help researchers to study spectroscopically the innermost parts of an outflow.

Key words: line: formation – radiation mechanisms: general – radiative transfer – stars: mass-loss – stars: winds, outflows – galaxies: active.

1 INTRODUCTION

It is widely accepted that radiation produced in the vicinity of compact objects can bear an imprint of the strong gravitational field, of either a stellar mass black hole (BH) or a neutron star (NS) in Galactic X-ray binary systems, or a supermassive BH in the case of active galactic nuclei (AGN). Thus the problem of direct detection of line emission from regions close to compact objects is of great importance. One of the most important piece of evidence for the presence of an accretion disc, and also the most extensively theoretically investigated subject in this field, is a broadened, redshifted spectral feature attributed to a fluorescent Kα emission line observed in the X-ray spectra of some Seyfert 1 galaxies. It is believed to be formed due to the reprocessing of X-rays emitted by the corona in the inner parts of a relatively cold accretion disc (see e.g. Fabian et al. 2000). If this is the case, then the line-forming region translates to a broad region in velocity and frequency space, making a line profile severely skewed by relativistic effects of the accreting plasma. This strong distortion of the spectral line makes detailed diagnostics of physical conditions in the plasma using this line difficult.

The grating spectrographs on the X-ray telescopes *Chandra* and *XMM–Newton* provide unprecedented spectral resolution up to $\sim$10 keV. Thus, by means of *Chandra* High Energy Grating observations, a narrow 'core' of the Fe Kα line was detected in many type 1 AGNs (Yaqoob & Padmanabhan 2005). In order to explain this spectral feature in these sources, it is necessary to invoke both reflection from an accretion disc and emission from distant regions (such as an obscuring torus).

Observations of several quasars and Seyfert galaxies reveal narrow X-ray absorption lines indicating matter outflowing, falling on to, and orbiting near the BH. These features are interpreted as Fe absorption lines, blue- and redshifted relative to the rest-frame frequency.

In some cases, observed spectral features are interpreted as being gravitationally redshifted absorption lines. Tentative evidence has been found for an absorption feature that presumably originates from resonant scattering of iron within an accretion flow in the strong gravitational field of the BH in the Seyfert 1 galaxy NGC 3516 (Nandra et al. 1999). In the paper by Yaqoob & Serlemitsos (2005) it was suggested that the detection of the narrow redshifted absorption line superimposed on the red wing of a broad Fe Kα line in the quasar E1821+643 is the result of resonance absorption by Fe XXV or Fe XXVI, gravitationally redshifted from a region within 10–20r_g from the BH. Reeves et al. (2005) interpreted an absorption features from the quasar PG 1211+143 as being produced by ionized iron and being Doppler redshifted due to either the plasma falling on to the black hole or gravitational redshifting, or both.

★E-mail: dora@milkyway.gsfc.nasa.gov

Matt et al. (2005) also reported on the possible detection of a transient absorption line from the ionized Fe from the quasar Q0056−363. If the observed redshift is only gravitational, then it has been argued that the absorbing gas lies within $\sim 5r_g$ from the BH. In the paper by Dadina et al. (2005), red- and blueshifted absorption lines are found in the X-ray spectrum of the Seyfert 1 galaxy Mrk 509. The data suggest that these features are formed in a flow moving with velocity $v \sim 0.15$–$0.2\,c$ or/and are gravitationally redshifted.

Much smaller astrophysical objects that may potentially demonstrate gravitationally redshifted lines are neutron stars. It is widely believed that X-ray bursts are produced as neutron stars are accreting plasma from their massive companions in close binary systems. It was also suggested that measurement of the gravitationally redshifted absorption lines during an X-ray burst can yield the mass-to-radius relation for the neutron star and thus provides the required constraint to the equation of state of the NS interior. Cottam, Paerels & Mendez (2002) reported on the observation of several absorption features in the X-ray burst spectra of the low-mass X-ray binary EXO0748−676. Prominent absorption features were attributed to the redshifted lines of Fe XXVI, Fe XXV and O VIII. It was speculated that both gravitational redshift and, possibly, a slow outflow are responsible for the observed features.

From the above examples one may conclude that there exists the possibility to observe gravitationally redshifted narrow spectral features from diverse classes of objects.

With the exception of a purely photospheric line, it is natural to assume that plasma that produces line emission is moving with respect to the source of radiation (photosphere or accretion disc).

The line-emitting plasma may be in the form of a diffuse wind and may or may not have a clumpy structure. In both cases one may hope to acquire important information from analysing the profiles of such lines, and to learn about the strength of the gravitational field, distance, velocity field etc.

Many normal, luminous stars possess strong mass loss. In many cases it is possible to derive information about the wind by analysing the P Cygni profiles formed in these winds. These peculiar profiles have long been known. The first paper that contained an explanation of P Cygni profiles on the basis of the Doppler effect was that of Beals (1931), who gave a basic explanation of the observed line profiles from novae and Wolf–Rayet stars. Since then, these profiles have been studied both observationally and theoretically in numerous papers. For example, Morton (1967) extensively investigated the P Cygni ultraviolet resonant line profiles from the winds of early supergiants.

A theoretical breakthrough was made in the paper by Sobolev (1960), in which he recognized that if there exists a velocity gradient along the line of sight, the radiation transfer problem becomes purely local. That is, distant regions in the flow can no longer exchange information using photons with frequencies within the width of the line. The radiation that is seen at a certain frequency within a line profile by a distant observer comes from a surface of equal line-of-sight velocity (see Section 3.1). Following this, significant attention has been paid to computing and analysing P Cygni profiles and also to investigating their dependence on fundamental parameters of the flow [see for example the atlas of P Cygni profiles by Castor & Lamers (1979)].

The main goal of this paper is to calculate the line profile produced by a plasma that is moving in the strong gravitational field of a compact object. Thus, we want to obtain an answer to the question of how much the gravitational redshifting can change the observed line profile in comparison with the standard case of a P Cygni line. Expecting that the gravitational redshifting may introduce some characteristic distortion to the P Cygni profile, we wish to investigate what kind of distortion is made and whether it can be used to deduce information about the wind and compact object system itself.

The layout of the paper is as follows: in Section 2 basic assumptions about the physical conditions and geometry of the line-forming region are described. Here the objectives and limitations of the approach are defined. In Section 3 we first calculate a spectral line optical depth, taking into account gravitational redshifting. This is done in the Sobolev approximation, which we adopt throughout the paper. In this Section equal frequency surfaces (EFS) are redefined to include the gravitational redshifting effect and the shapes of such surfaces are calculated for several typical velocity profiles. The results obtained in this Section are extensively used in the calculation of the radiation field within a spectral line in Section 4 and the numerical calculation of line profiles in Section 5. At the end of the paper we provide a discussion and summarize the results.

2 ASSUMPTIONS

As mentioned above, the problem we address in this paper may be relevant to various astrophysical objects. Physical conditions in the wind driven from the accretion disc in AGN are different from those in the outflowing plasma during an X-ray burst. At the same time we would like to elucidate some new features that may arise in a spectral line profile when the influence of the gravitational field is non-negligible. As a zero-order model we adopt the simplest geometry and make further hypotheses about the velocity profile, temperature distribution, opacity etc. We wish to consider a minimum number of free parameters, as their overabundance will likely obscure rather than elucidate the origin of expected new features. We make the following assumptions about the geometry and kinematical properties of the absorbing plasma and the source of continuum photons.

(i) The velocity distribution is spherically symmetric. This assumption allows a simplification to the radiation transfer problem and also adds robustness to the results. In some cases a departure from spherical symmetry (e.g. the wind from an accretion disc) should be taken into account. For example, rotation may have some influence on the line profile. However, in radiationally or thermally driven accretion disc winds, the radial component of the velocity can quickly exceed the toroidal component, owing to the conservation of the angular momentum. Notice that this may not be the case in magnetohydrodynamics (MHD) winds, in which the poloidal velocities may not be much larger than the toroidal ones, e.g. Blandford & Payne (1982). On this ground we hypothesize that inclination and geometrical effects arising from accretion discs may have more influence on the resultant line profile.

(ii) The velocity profile is represented by a gradually increasing function of the radius. In the case of P Cygni profiles from normal stars, decelerating winds were considered in several works (see e.g. Marti & Noerdlinger 1977). Some results of these papers are discussed further in the text.

(iii) The only source of continuum photons is the spherical core. An accretion disc may influence the results in two ways: close to the BH, the disc provides a strongly anisotropic radiation field; also the disc may screen the emission from part of the wind. At the end of this paper we investigate the effect of screening by a disc that is viewed face-on.

(iv) No bending of the photon trajectories is taken into account. While this effect plays an important role in formation of lines from

the inner parts of accretion discs (both Schwarzschild and Kerr) it does not play an important role in the 'zero-order' model adopted in this paper. The relative importance of bending can be inferred from the equation that describes the orbit of a photon in the gravitational field of a Schwarzschild BH:

$$\frac{1}{x} \simeq \sin\alpha + \frac{1}{4g_0}(3+\cos 2\alpha), \tag{1}$$

where α is the polar angle of the photon trajectory with the impact parameter b, $g_0 = b/r_g$, $r_g = 2GM/c^2$ is the Schwarzschild radius and $x = r/b$. In the current studies we are concerned with the regions of the flow located approximately at radii $>10r_g$. Thus, taking $x = \infty, g_0 \sim 20$ we obtain the deflection angle $\Delta\alpha \simeq 5\overset{\circ}{.}7$. Taking into account bending of photon trajectories would introduce a significant complication in the solution of the radiation transfer problem and would require frequency-dependent Monte Carlo simulations of the radiation transfer in the frame of general relativity (GR), which is beyond the scope of the current study.

3 OPTICAL DEPTH

We associate an observer situated at infinity, O^∞, with the laboratory frame ('lab' for short). The fluid we consider is moving with the velocity v. It is most convenient to measure absorption and emission coefficients in the comoving frames, $O_{\rm com}$, coinciding instantaneously with the fluid at each point along the streamline. To obtain a relation between these two frames one needs to consider another local frame, $O_{\rm loc}$, a Lorentzian frame that is at rest at a given point s_0 and instantly coincides with the $O_{\rm com}$ frame. Generally $O_{\rm loc}$ and O^∞ are not the same because of the presence of the gravitational field. The opacity in the $O_{\rm loc}$ frame is obtained according to the transformation $\chi^l_{\rm loc} = \chi^l_{\rm com}\,\tilde\nu/\nu_{\rm loc}$, where $\chi^l_{\rm com}$ and $\tilde\nu$ are the absorption coefficient and the frequency of the radiation in the comoving frame. Notice that we neglect all effects associated with the strong gravitational field except for the change of the radiation frequency. In particular, we assume that photons are propagating in straight lines, so that $\mu_{\rm lab} = \mu_{\rm loc}$, where μ is the cosine of an angle between the radius vector and the direction of the ray. The frequency of a photon that is propagating in the background gravitational field can be found from the relation $\nu_{\rm loc}\sqrt{g_{00}} = $ constant (Landau & Lifshitz 1960), where g_{00} is the corresponding component of the Schwarzschild metric tensor. In the 'weak field limit' it follows that $\sqrt{g_{00}} \simeq 1 + \phi/c^2$, where $\phi(r)$ is the potential of the gravitational field.

In this paper, we adopt the pseudo-Newtonian potential of Paczynski and Wiita (PW) (Paczynski & Wiita 1980):

$$\phi(r) = \frac{GM}{r_g - r}. \tag{2}$$

The PW potential mimics important features of exact general relativistic solutions for particle trajectories near a Schwarzschild black hole. This potential correctly reproduces the positions of both the last stable circular orbit, located at $3r_g$, and the marginally bound circular orbit at $2r_g$. This useful property, to capture the essentials of GR effects, has been used in Dorodnitsyn (2003) to calculate the structure of the line-driven wind near a compact object, and the results are in good agreement with the GR calculations of Dorodnitsyn & Novikov (2005).

The Lorentz transformations between $O_{\rm loc}$ and $O_{\rm com}$ give $\tilde\nu = \gamma\,\nu_{\rm loc}(1-\mu\beta)$, where $\beta \equiv v/c, \gamma \equiv (1-\beta^2)^{-1/2}$. Consider a photon that is emitted at a point s_0. At some other point s its comoving frequency is

$$\tilde\nu(s) = \gamma\,\nu_{\rm loc}(s_0)\sqrt{g_{00}(s_0)/g_{00}(s)}[1-\mu(s)\beta(s)].$$

In order to allow for moderately high terminal velocities we will write all equations out to the second order, i.e. retain terms β, β^2 and ϕ/c^2. Taking into account that $\nu_{\rm loc}(s_0)\sqrt{g_{00}(s_0)} = \nu^\infty$, where ν^∞ is the frequency measured by the observer O^∞, we obtain

$$\tilde\nu(s) = \nu^\infty\left(1 - \mu(s)\beta(s) - \frac{\phi(s)}{c^2} + \frac{\beta(s)^2}{2}\right). \tag{3}$$

The probability of emitting a photon within a frequency range $(\tilde\nu,\ \tilde\nu + {\rm d}\tilde\nu)$, and within a range of solid angles in the comoving frame $(\tilde\Omega,\ \tilde\Omega + {\rm d}\tilde\Omega)$ is

$${\rm d}P_e = (4\pi)^{-1}\,\Psi(\tilde\nu - \nu_0)\,{\rm d}\tilde\nu\,{\rm d}\tilde\Omega,$$

where ν_0 is the frequency of the line in the comoving frame, and the line profile function Ψ is assumed to obey the normalization condition $\int_0^\infty \Psi(\tilde\nu - \nu_0)\,{\rm d}\tilde\nu = 1$.

The optical depth between a point s and $+\infty$ along the photon trajectory, which is a straight line in our approximation, is calculated adopting a transformation from space to frequency variables:

$$t = \int_s^\infty \chi^l_{\rm loc}\,{\rm d}s' = \int_s^\infty \frac{\tilde\nu(s')}{\nu_{\rm loc}}\chi^l_{0,\rm com}\Psi\,(\tilde\nu - \nu_0)\,{\rm d}s'$$
$$= \int_{\tilde\nu(s)}^{\tilde\nu(\infty)} \frac{\tilde\nu}{\nu_{\rm loc}}\chi^l_{0,\rm com}\frac{\Psi\,(\tilde\nu - \nu_0)}{\left(\dfrac{{\rm d}\tilde\nu}{{\rm d}s}\right)_{s'}}{\rm d}\tilde\nu, \tag{4}$$

where $\chi^l_{0,\rm com}$ is the line-centre opacity in the comoving frame:

$$\chi^l_{0,\rm com} = \frac{\pi e^2}{mc}(gf)\frac{N_{\rm l}/g_{\rm l} - N_{\rm u}/g_{\rm u}}{\Delta\nu}, \tag{5}$$

where $N_{\rm u}, N_{\rm l}$ and $g_{\rm u}, g_{\rm l}$ are respectively populations, statistical weights of the corresponding levels of the line transition, f is the oscillator strength of the transition, $\Delta\nu = \nu_0\,v_{\rm th}/c$ is the Doppler line width, and $v_{\rm th}$ is the thermal velocity. Given the Sobolev approximation we assume that a photon, after being scattered in a line at a point s_0, can further interact with matter only in the immediate vicinity of this point. Owing to gradients of the velocity and gravitational potential, such a photon is quickly shifted out of resonance with the line. We expand $\tilde\nu$ in the vicinity of s_0 as a Taylor series retaining two terms in $(s - s_0)$:

$$\tilde\nu(s) \simeq \tilde\nu(s_0) + \left(\frac{{\rm d}\tilde\nu}{{\rm d}s}\right)_{s_0}(s - s_0) + \frac{1}{2}\left(\frac{{\rm d}^2\tilde\nu}{{\rm d}s^2}\right)_{s_0}(s - s_0)^2. \tag{6}$$

Usually in the Sobolev approximation only the first-order term is left in (6), and in most cases this is sufficient. However, there are some pathological situations, namely a singularity in (4), in which the second-order term in the equation (6) is required.

Using relations (4) and (6) and taking into account that in the Sobolev approximation the opacity is considered to be constant throughout the resonant region, the expression (4), to the second-order v^2/c^2, reads:

$$t \simeq \tau_0(\mu, s)\left[1 + \beta^2(1+\mu^2) - 2\mu\beta - \frac{\phi}{c^2}\right]\zeta(\tilde\nu), \tag{7}$$

where

$$\tau_0(\mu, s) \simeq \chi^l_{0,\rm com}/|Q(\mu, s)|, \tag{8}$$

and

$$Q(\mu, s) = \alpha_1 + \alpha_2\,\Delta s, \tag{9}$$

where

$$\alpha_1 \equiv (\nu^\infty)^{-1}\left(\frac{{\rm d}\tilde\nu}{{\rm d}s}\right)_s, \quad \alpha_2 \equiv (\nu^\infty)^{-1}\left(\frac{{\rm d}^2\tilde\nu}{{\rm d}s^2}\right)_s, \tag{10}$$

and $\Delta s = s' - s$, where s' is a point located on the trajectory of the photon. In practice, we take $\Delta s =$ constant. This quantity is required in order to evaluate numerically the optical depth in those directions μ at which $\mathrm{d}\tilde{\nu}/\mathrm{d}s$ vanishes (see the discussion later in this Section). The second factor in (7), $\zeta(\tilde{\nu})$, reads

$$\zeta(\tilde{\nu}) = \int_{\nu_0-1/2}^{\tilde{\nu}} \Psi(\tilde{\nu} - \nu_0)\,\mathrm{d}\tilde{\nu}. \tag{11}$$

For simplicity we assume that the line absorption coefficient is zero outside the frequency interval $(\nu_0 - \Delta\nu/2, \nu_0 + \Delta\nu/2)$ i.e. in terms of $\Delta\nu$ the spectral line has a half-thickness of 1/2. In equation (7), it was assumed that $(\nu^\infty)^{-1} \simeq (\nu_0)^{-1}\,(1 + \beta^2/2 - \mu\beta - \phi/c^2)$.

We integrate the radiation transfer equation along characteristics, which in spherical symmetry are the rays of constant impact parameter p. Differentiating in a direction of $\boldsymbol{s} = z\hat{\boldsymbol{z}}$, we consider all dependent variables as either functions of (r, μ) or (p, z). Taking into account that $\frac{\mathrm{d}}{\mathrm{d}s} = \left(\frac{\partial}{\partial z}\right)_p = \frac{1-\mu^2}{r}\frac{\partial}{\partial \mu} + \mu\frac{\partial}{\partial r}$, $\mu = z/\sqrt{p^2+z^2}$ and $r = \sqrt{p^2+z^2}$, we find

$$-(\nu^\infty)^{-1}\frac{\mathrm{d}\tilde{\nu}}{\mathrm{d}s} = \frac{\beta}{r}\left[1 - \mu^2\left(1 - \frac{\mathrm{d}\ln\beta}{\mathrm{d}\ln r}\right) + \mu\left(\frac{1}{\beta c^2}\frac{\mathrm{d}\phi}{\mathrm{d}\ln r} - \beta\frac{\mathrm{d}\ln\beta}{\mathrm{d}\ln r}\right)\right]. \tag{12}$$

Similarly, after some algebra we find

$$-(\nu^\infty)^{-1}\frac{\mathrm{d}^2\tilde{\nu}}{\mathrm{d}s^2} = \left[\frac{1-\mu^2}{r}\left(\frac{2\mu\beta}{r} + \beta'(\beta - 2\mu) - \frac{\phi'}{c^2}\right) + \mu\left\{\frac{1-\mu^2}{r}\left(\frac{\beta}{r} - \beta'\right) + \mu\left[(\beta')^2 - \mu\beta'' + \beta\beta'' - \frac{\phi''}{c^2}\right]\right\}\right], \tag{13}$$

where the prime denotes differentiation with respect to r.

In classical Sobolev theory, $\mathrm{d}\tilde{\nu}/\mathrm{d}s$ appears to be an even function of μ. In our case a situation is possible where, for certain values of μ, Doppler shifting and gravitational shifting cancel each other, zeroing the right-hand side of equation (12). Note that even if the $\mu\phi'$ term in (12) is taken away the right-hand side of this equation can change sign depending on whether $\mathrm{d}v/\mathrm{d}r$ is positive or negative if radius is increased. Thus for *decelerating* flows it is possible that a purely geometrical frequency shift, $[(1-\mu^2)/r]v$ (arising from the divergence of the spherically symmetrical fluid flow), can compensate for the $\mu^2 v'$ term.

Strictly speaking, for those directions of μ at which gravitational frequency shifting cancels Doppler shifting, the first-order [in $(s - s_0)$] Sobolev approximation is formally not applicable because of the singularity found in the denominator of equation (8). A similar problem has also been found by Jeffery (1995), who considered the relativistic, time-dependent Sobolev approximation. In practice, when numerically evaluating the integral (4) we adopt the following procedure. In most cases the first-order Sobolev approximation works very well and only the term that is first-order in $(s - s_0)$ has been retained in (8). In our calculations, in most cases the singularity in (4) has not been detected. On the other hand, in those rare situations when it was found we have taken the second-order term into account in the denominator of (7). Doing so, we use a second-order expansion (6), and additionally specify a *constant* value of Δs. It should be emphasized that our experiments in choosing different values of Δs persuaded us that the resultant line profile is not influenced by this choice.

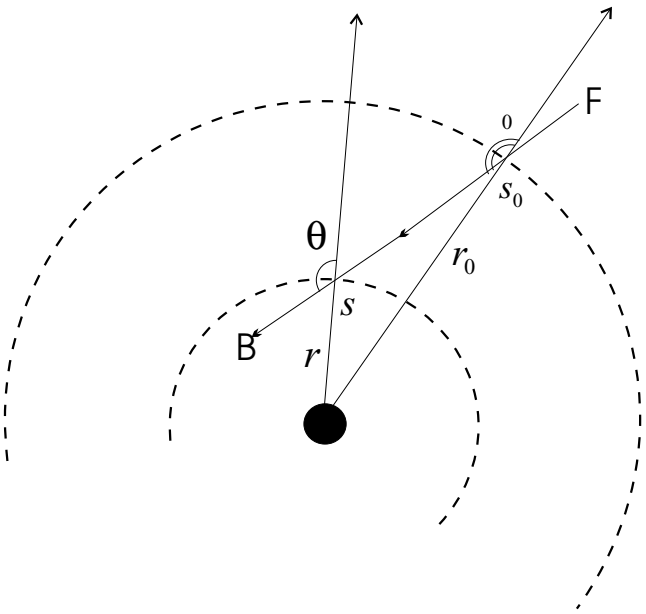

Figure 1. A photon propagating in arbitrary direction FB from larger to smaller radii. A wind moves radially with the velocity $V(r)$. Corresponding projections of the radial velocity on the direction of the ray at points s_0 and s determine the relative Doppler shifting. For certain cases the latter can compensate for the gravitational shifting between these two points (see e.g. the discussion before and after equation 14).

To understand better the physical origin of the singularity, it is instructive to consider a ray formed by photons propagating from larger to smaller radii, i.e. from $r(s_0)$ to $r(s)$ in the direction FB as depicted in Fig. 1. Assuming the velocity field to be spherically symmetric and the velocity gradient to be positive, $\mathrm{d}v/\mathrm{d}r > 0$, and denoting $\mu(s_0) = \cos\theta_0$ and $\mu(s) = \cos\theta$, one can see that there are two cases to be considered: (i) $\mu(s_0) < \mu(s) < 0$, so that

$$|\mu(s_0)| > |\mu(s)|, \tag{14}$$

and (ii) $\mu(s_0) < 0, \mu(s) > 0$. Rewriting equation (3) and keeping only first-order terms, we obtain

$$\delta\nu/\nu_0 = -\left[\beta(s_0)|\mu(s_0)| \mp \beta(s)|\mu(s)|\right] + \frac{|\phi(s)| - |\phi(s_0)|}{c^2}, \tag{15}$$

where $\delta\nu \simeq \tilde{\nu}(s) - \nu_0$, $\tilde{\nu}(s_0) \simeq \nu_0$ and the minus sign corresponds to the case (i). If $r(s) < r(s_0)$, and recalling that velocity is an *increasing* function of r, we obtain $\beta(s_0) \geq \beta(s)$. Since the last term on the right-hand side of (15) is positive, we see that in both cases it can compensate for the term arising from the Doppler shift. That is, in contrast to the case when no gravitational redshifting is taken into account, here a photon emitted in the wind can again interact within the wind, thus providing a radiative coupling of distant points. Thus we arrive at the problem of multiple-valued equal frequency surfaces.

The problem of multiple-branched equal velocity surfaces is known from the modelling of line profiles from decelerating atmospheres (Kuan & Kuhi 1975; Surdej 1977). These authors adopted a decelerating velocity law, $v(r) = V_{\mathrm{constant}}(R_{\mathrm{ph}}/r)^l$, where $l > 0$ is a parameter of deceleration and R_{ph} is the radius of the photosphere. For such a velocity distribution, a coupling of distant points owing to the zero relative frequency shift is found. As a result of such coupling, the radiation field at any of these points includes a contribution not only from the source of continuum radiation ('core') but also from distant parts of the flow.

3.1 Surfaces of equal frequency

It is convenient to introduce a non-dimensional frequency variable that measures a displacement of the frequency from that of the line centre in terms of Doppler line width, $\Delta\nu$:

$$y = (\nu - \nu_0)/\Delta\nu. \tag{16}$$

Similarly, a comoving version of this variable reads $\tilde{y} = (\tilde{\nu} - \nu_0)/\Delta\nu$, and for the observer, O^∞, we obtain $y^\infty = (\nu^\infty - \nu_0)/\Delta\nu$ as a measure of the red-/blueshift within the line profile. According to the Sobolev approximation, photons of a certain frequency emitted in a spherically symmetric, gradually accelerated atmosphere may come only from the volume occupied by a thin shell of thickness $l(p, z) \sim v_{\rm th}/({\rm d}v/{\rm d}r)$. In the limit $\Psi(\tilde{y}) = \delta(\tilde{y})$, this shell becomes a surface of constant line-of-sight velocity. This is a key idea behind the calculation of the line profiles in the Sobolev approximation. The concept of surfaces of constant line-of-sight velocity, $v\cos\theta$, can be modified and expanded to account for gravitational redshifting. In such a case they are better referred to as equal frequency surfaces (hereafter EFS). Similarly to how the relation (3) was obtained, we write

$$y^\infty - \tilde{y} = \Delta\nu^{-1}(\nu^\infty - \tilde{\nu}) = \mu u + \Phi - u^2/(2\zeta), \tag{17}$$

where $u = v/v_{\rm th}$ is the non-dimensional velocity, $\zeta = c/v_{\rm th}$ and $\Phi = \phi/(cv_{\rm th})$ is the non-dimensional potential.

A photon of the emitted frequency ν_0 (i.e. $\tilde{y} = 0$), emitted in the wind at a point (z_0, p), has at infinity an observed frequency y^∞. Then an equation for the resonant surfaces reads

$$y^\infty - \frac{z_0}{\sqrt{z_0^2 + p^2}} u\left(\sqrt{z_0^2 + p^2}\right) + \Phi\left(\sqrt{z_0^2 + p^2}\right) - \frac{1}{2\zeta} u^2\left(\sqrt{z_0^2 + p^2}\right) = 0. \tag{18}$$

This equation determines the locus of the equal frequency surface (i.e. z_0) as a function of p and y^∞. The non-dimensional form of the PW potential (2) reads $\Phi(x) = \zeta/2(1 - xg_0)$, where $x = r/R^*$ is the non-dimensional radius, and R^* is the radius of the spherical core from which the wind is launched. A non-dimensional parameter, $g_0 = R^*/r_{\rm g}$, determines the relative importance of gravitational redshifting (i.e. by equating $g_0 \to \infty$ one completely neglects the influence of the gravitational field on the energy of a photon). Equation (18) may have multiple roots z_{0i} depending on the values of y^∞ and p and the velocity law. For the range of parameters relevant to this work, it is possible to show that the last term in (18) does not affect the overall properties of this equation. It is also true that for a given impact parameter, p, and for any reasonable velocity profile $v(r)$ (i.e. a smooth single-valued *increasing* function of r), the following cases should be considered separately.

(i) Blueshifting domain, $y^\infty \geq 0$: equation (18) may have zero or one root. The latter may be located only at positive z (which implies that if $z \geqslant 0$, the superposition of Doppler blueshifting and gravitational redshifting can result in the observable $\nu^\infty(y^\infty)$ only for unique z_0, p).

(ii) Redshifting domain, $y^\infty < 0$: the situation is more complicated, as equation (18) may have zero, two or three roots. At $z \geq 0$ there is always one (gravitational redshifting is stronger than Doppler blueshifting) or no root. At $z < 0$, depending on the velocity law there can be a situation in which a superposition of gravitational and Doppler redshifting at some radius r_1 (at which gravity is stronger but the velocity is small) can equalize the sum of Doppler and gravitational redshifting at some larger radius, $r_2 > r_1$ (i.e. where gravity is negligible but velocity is high).

The shape of the resonant surfaces varies depending on the velocity profile. We can understand their shapes by considering only a few characteristic cases for $v(r)$. These cases are as follows.

(i) $v = 0$. This case makes sense if $g_0 \neq 0$, i.e. a photon is redshifted by the gravitational field of a central object. From (17) the maximum gravitational redshift is $y_{\rm min} = (\zeta/2)(1 - x\,g_0)^{-1}$. For a given y^∞, the EFS has the shape of a sphere of radius $x(y^\infty) = g_0^{-1}[1 - \zeta/(2y^\infty)]$.

(ii) $v =$ constant. An example would be the outer part of a stellar wind in which the flow is approaching terminal velocity and moves at almost constant speed. Alternatively, considering a spectrum from a thin, moving shell one may approximate the distribution of velocity within such a shell as constant. In the case of negligible gravitational redshifting, the condition $V_z = \mu v =$ constant, where V_z is the velocity projected on the line of sight, determines the locus of the EFS. Thus if $v =$ constant the EFS has a conical shape. An intersection of this EFS with the p–z plane consists of two straight lines passing through the centre and being symmetrical about the z-axis. Even in the case of $g_0 \to 0$ and $v =$ constant there is a frequency shift along the line of sight originating from the divergence of the flow lines in spherically symmetrical geometry (see e.g. equation 12).

(iii) $v \sim$ constant $\times\, r$. Another name for this dependence is a 'Hubble law', which describes explosive events, in which more rapidly moving particles at large radii are outrunning the slower moving ones at small radii.

To understand qualitatively real winds, for example those that are quickly escaping from the potential well (as does a line-driven wind in an O star) one may approximately consider their non-linear velocity profile as being linear, $v \sim r$ in the inner part and $v \sim$ constant in the outer part of the flow.

Fig. 2 shows equal frequency surfaces for the velocity law

$$u(x) = U^\infty(x - 1)/(x_{\rm t} - 1), \tag{19}$$

where $U^\infty = V^\infty/v_{\rm th}$, V^∞ is a terminal velocity, $x_{\rm t} = R_{\rm t}/R^*$, and $R_{\rm t}$ is the wind terminating radius, $R_{\rm t} = 100\ R^*$. Thus, if $u(x) \simeq U^\infty x/x_{\rm t}$ and $g_0 \to \infty$ (i.e. no gravitational redshifting) one finds from (18) that EFS is determined by the condition $z = R_t\, y^\infty/U^\infty$. Notice that in Fig. 2 the equal redshift surfaces for the blueshifted photons are parametrized in terms of $y_{\rm max} = U^\infty$ (i.e the maximum blueshift in the case of $g_0 \to \infty$) . The shape of these surfaces resembles that obtained in the case of $g_0 \to \infty$.

The most important difference from the case when $g_0 \to \infty$ is the appearance of multi-valued surfaces at the single frequency y^∞. As was already mentioned, when $y^\infty < 0$ (redshifting), equation (18) may have one root at positive z and two roots at $z < 0$. As an example, consider a case when $y^\infty = 0.2\, y_{\rm min}$. There are two equal redshift surfaces: an ellipsoid-like surface at small r and a plane-like surface at larger radii (Fig. 2, left panel). At larger redshift, $y^\infty = 0.3\, y_{\rm min}$, the inner surface shrinks to smaller r, where the gravitational potential is stronger, while the outer surface shifts to larger r, to the domain where the velocity and the corresponding Doppler redshift are larger.

Terminal velocity 0.01 c is too small to describe a continuous flow from such a small radii as $R^* = 25\, r_{\rm g}$. However, physical conditions in the flow (most importantly, the ionization state in the gas) should allow for the formation of lines from heavy ions and at the same time have enough column density to shield these ions from being completely ionized. In other words, when conditions to form the line are just right only in a given part of a flow, and where the velocity may be approximated by the linear dependence.

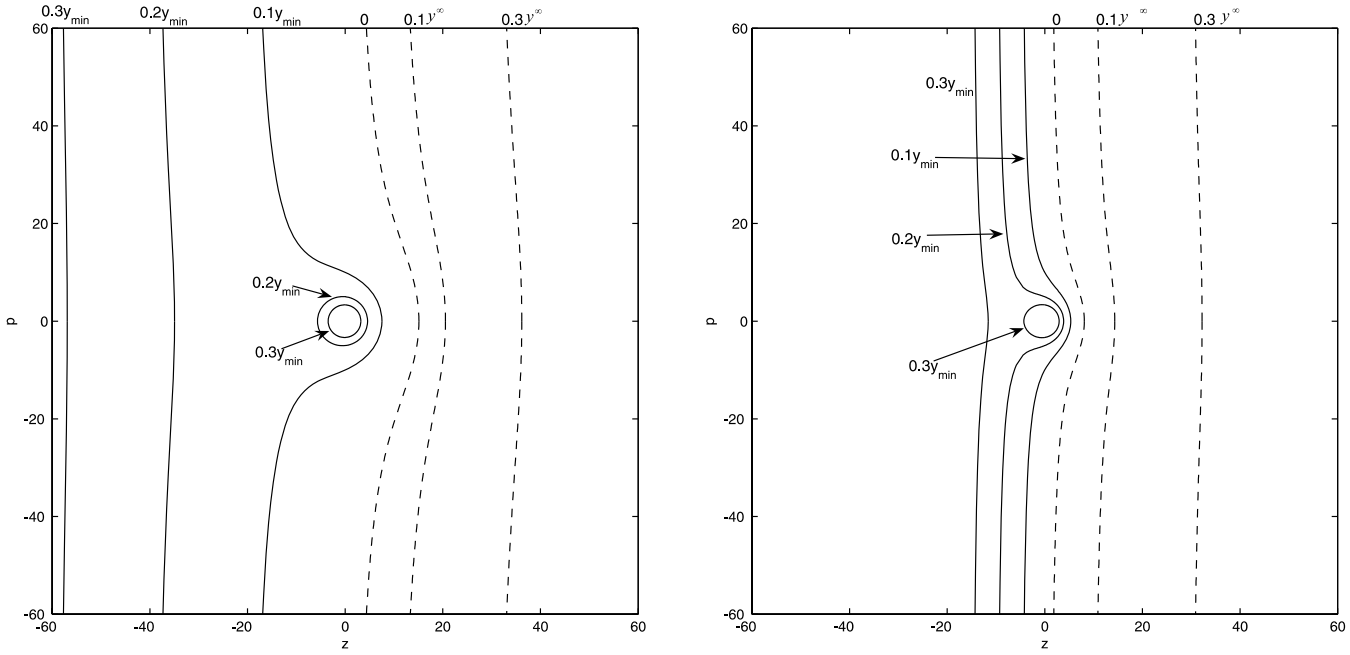

Figure 2. Equal frequency surfaces for the velocity law (19). The parameters are $R^* = 25r_g$ and $V^\infty = 0.01\ c$ (left) and $R^* = 10r_g$ and $V^\infty = 0.1\ c$ (right). Notice that a surface of equal frequency can have several branches, e.g. a ray with a given ν^∞ and p can intersect it up to three times (see text for details). The observer is located at $z \to \infty$.

For example, if the opacity peaks at small radii within a continuous flow, an effective maximum velocity in this shell-like region is much smaller than V^∞. The low terminal velocity case is only applicable if the absorption takes place only at the low-velocity base of the wind.

In a general case, we expect that a transonic stellar wind should have a terminal velocity of the order of the escape velocity at the wind launching point. For example, for the parameters in this paper, the escape velocity is of the order 0.2– 0.3 c. Fig. 2 (right panel) shows such EFS for $V^\infty = 0.1\ c$.

(iv)

$$v = V^\infty \sqrt{1 - \frac{R^*}{r}}. \tag{20}$$

This is a typical velocity profile for the transonic wind that is launched deep in a potential well. Such a wind is characterized by a steep transonic region, containing a critical point or multiple critical points (as in the case of line-driven winds), and an extended plateau where the velocity approaches V^∞. This type of velocity law is usually considered to approximate gradually accelerated atmospheres of hot stars.

The characteristic behaviour of the EFS in this case can be understood from the previously considered cases: $v \sim$ constant and $v \sim r$. Fig. 3 shows the EFS for the parameters $V^\infty = 0.1\ c$ and $R^* = 15r_g$. One can see that the shape of the EFS is mostly affected by the outer part of the flow, i.e. where $v \sim V^\infty$, rather then by the inner 'acceleration' part. The latter is more important for the EFS obtained for $V^\infty = 0.01\ c$ (i.e. as in Fig. 4).

Summarizing, we note that gravitational redshifting adds new ingredients to the classical topic of surfaces of equal frequencies.

(1) Equal frequency surfaces for the redshifted part of the spectrum ($y^\infty < 0$) may be located both in front of and behind the compact object. Equal redshift surfaces can break suddenly as the impact parameter approaches some critical value.

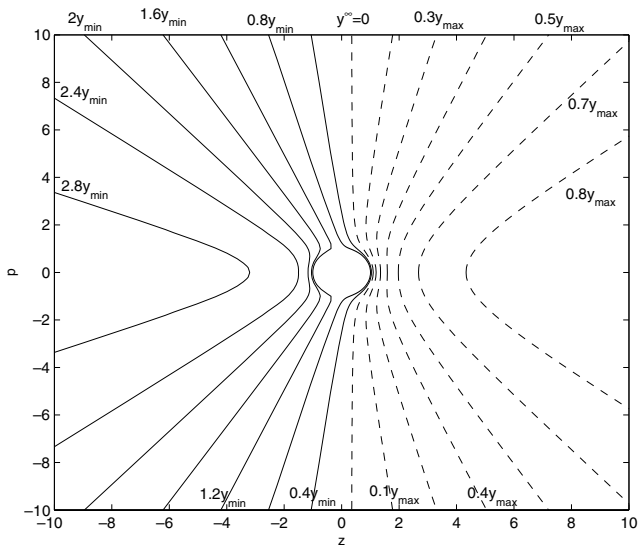

Figure 3. Equal frequency surfaces for velocity law $v(r) = V^\infty \sqrt{1 - R^*/r}$, where $V^\infty = 0.1\ c$ and $R^* = 15r_g$.

(2) For $y^\infty < 0$ the EFS may have a closed (ellipsoid-like) form. A ray with impact parameter p and frequency y^∞ may cross resonant surfaces several times depending on the velocity law and on the relative importance of gravity, i.e. proximity to the compact object.

Physical conditions (i.e. ionization balance, radiation field) that affect the formation of a particular portion of the line profile are very different on different branches of the EFS. For example, in the simple case of $v \sim r$ the absorption part is affected by the EFS that resides close to the photosphere, while the emission part is created by an EFS that may be located quite far from the photosphere (because of the large surface area of such a surface). The same may

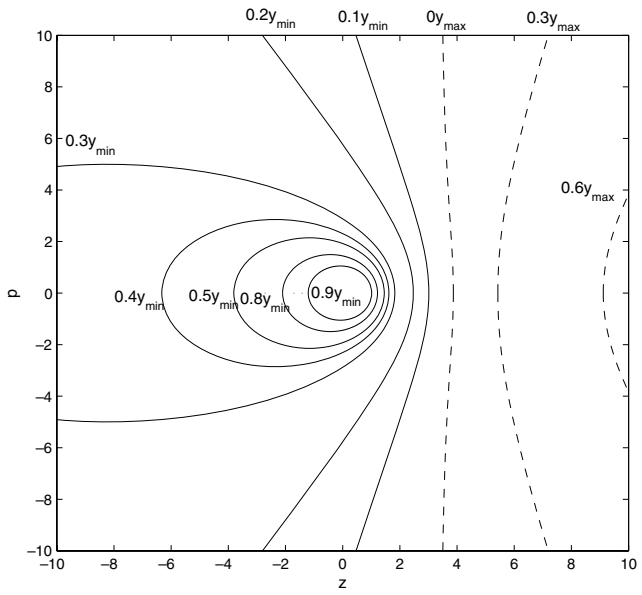

Figure 4. The same problem as in Fig. 3, but parameters of the flow are different: $V^{\infty} = 0.01\ c$ and $R^{*} = 15 r_{\rm g}$.

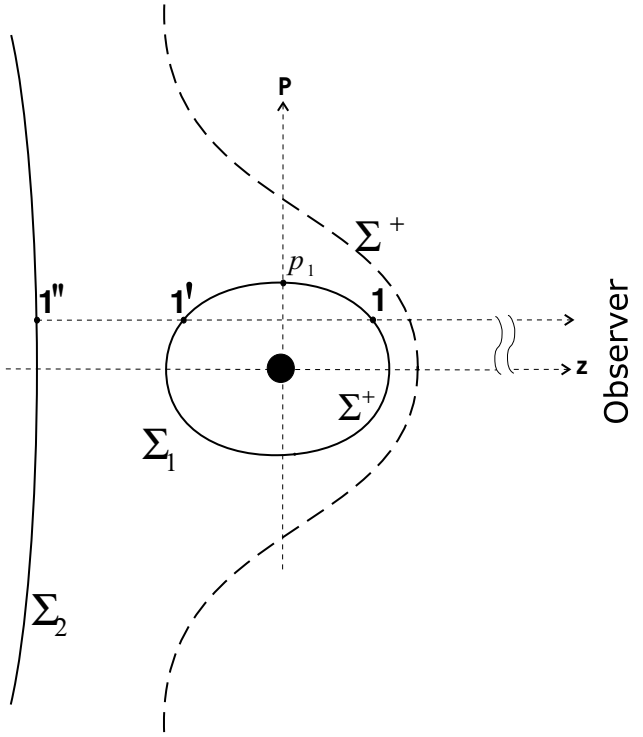

Figure 5. Illustration of the geometry of equal frequency surfaces (see text for details). Not to scale.

hold true for some other velocity profiles (see Section 5). Having said this, we proceed to the next section and prepare final formulae for the calculation of line profiles.

4 RADIATION FIELD IN A LINE

The mean radiation field J at any point on the EFS consists of photons emitted by atoms in the immediate vicinity of this point: a local contribution, $J_{\rm loc}$, and a contribution from distant points, $J_{\rm dist}$. The latter consists of photons emitted by the core, $J_{\rm core}$, and photons that arrive from other branches of the EFS. We assume the intensity $I_{\rm c}$ emitted by the core is constant over the line frequency interval $(\nu_0 - \Delta\nu/2,\ \nu_0 + \Delta\nu/2)$, with no limb darkening taken into account.

In the presence of resonant surface Σ_i the calculation of the intensity is straightforward. The non-local Sobolev approximation was mainly developed in the papers by Grachev & Grinin (1975) and Rybicki & Hummer (1978).

After being either emitted by the core or rescattered by another EFS, the intensity remains constant along the ray $\boldsymbol{s}$ until it encounters the EFS at s_i, where it changes discontinuously according to the relation (see e.g. Rybicki & Hummer 1978)

$$I^{s_i+0} = I^{s_i-0} {\rm e}^{-\tau_{\Sigma_i}} + S_{\Sigma_i} \left(1 - {\rm e}^{-\tau_{\Sigma_i}}\right). \qquad (21)$$

The situation is illustrated in Fig. 5. In this figure $\Sigma^{\pm}$ refers to the surface of equal frequency, and the '$-$' or '$+$' sign denotes whether the corresponding part of the EFS is located at $z < 0$ or at $z > 0$, respectively. As was already established, the EFS may have a closed or open shape. Thus Fig. 5 represents a situation in which gravitational redshifting is important and there are two branches of the EFS: a closed, ellipsoid-like one, and a plane-like one at larger r (smaller z), cf. Fig. 2. The second possibility is that the two branches of the EFS are both open surfaces. (To illustrate this point we draw such a surface, Σ^{+}, as a dashed line). The other notation in the figure has the following meaning: Σ_1^{-} is a negative part of that branch that has a closed form and Σ_2^{-} is a negative and open part of the multiple-branch surface.

The mean radiation field at point 1 is contributed by photons arriving from the core and from surfaces Σ_1^{-} and Σ_2^{-}. Photons emitted by Σ_1^{-}, if not occulted by the core, may be attenuated by the line scattering only locally to the point 1:

$$J \sim \int_{\Omega'} I_1(\Omega) \beta_{\rm loc}^1 \, {\rm d}\Omega,$$

where I_1 is the radiation intensity coming from points on $\Sigma^{-\prime}{}_1$ seen from point 1 within the solid angle Ω' occupied by the unobscured part of $\Sigma^{-\prime}{}_1$. One should note that the resonance surface that is seen from point 1, for example, $\Sigma^{-\prime}{}_1$ *is not* Σ_1^{-} but a different EFS. In a general case it should be calculated separately for each point where J is calculated. The same remains true for all other possible branches of EFS that can contribute to the mean radiation field at a given point. Generally speaking, Fig. 2 only shows that screening is possible. The goal of taking all these geometrical effects into account is beyond the scope of this paper. However, when calculating the radiation field at point 1 one may want to take into account contributions *only* from points $1'$ and $1''$, i.e. only from those points that are situated on the ray $(p,\ y^{\infty})$. Their positions remain unchanged and this fact greatly simplifies calculations. This is the first simplification in our description of the radiation field.

The second simplification arises from the ignorance of possible mutual screenings of the EFS between each other and a core (see discussion below). The probability for a photon to penetrate to point 1 without being scattered in its immediate vicinity can be cast in the form

$$\beta_{\rm loc}^1 = \left(1 - {\rm e}^{-\tau(\Sigma^{+})}\right) \Big/ \tau(\Sigma^{+}).$$

The intensity can be determined from the following relation:

$$I_1(1') = S(1') \left(1 - {\rm e}^{-\tau(1')}\right),$$

where $S(1')$ is the source function at the point $1'$ on Σ_1^-. Analogously a contribution from $1''$ can be constructed.

Radiative coupling between different branches of EFS poses a difficult problem to treat self-consistently. To overcome this difficulty, different authors adopt different approximations. When considering radiative coupling between fiducial points s and s' Grachev & Grinin (1975) have ignored the variation of the source function, assuming that $S(s') = S(s)$. Another approximate approach was adopted by Kuan & Kuhi (1975) who ignored the radiative coupling between s and s'. In the literature this is known as the 'disconnected approximation' (Marti & Noerdlinger 1977). Giving an extensive analysis of the problem of interconnection of different EFS branches for *decelerating* flow, these authors arrive at the conclusion that (i) taking into account radiative coupling can be of importance for the calculation of the radiation force; (ii) fortunately, the disconnected approximation of Kuan & Kuhi (1975), which completely neglects such coupling, works well and gives generally correct results for the source function and resultant profiles.

In this paper the appearance of additional branches of the EFS is treated in the spirit of the 'disconnected approximation'. For example, when calculating mean intensity at point $1''$ of Fig. 5, we neglect any contribution from those resonant points that could be located on the line from the core to this point. These could have important consequences because of the possible screening effect. In turn this would affect the emission part of the spectrum. To simplify the treatment we also assume that the core serves as the only source of photons that contributes to J at a given point. For simplicity we assume that the core is radiating with constant intensity I_c. The intensity of the radiation at $r \to \infty$ at a given impact parameter p and with a given frequency y^∞ is

$$\begin{aligned} I^\infty(y^\infty, p) = {} & I_c e^{-\tau(\Sigma^+)} + S(\Sigma^+)\left(1 - e^{-\tau(\Sigma^+)}\right) \\ & + S(\Sigma_1^-)\left(1 - e^{-\tau(\Sigma_1^-)}\right) e^{-\tau(\Sigma^+)} \\ & + S(\Sigma_2^-)\left(1 - e^{-\tau(\Sigma_2^-)}\right) e^{-\left(\tau(\Sigma^+)+\tau(\Sigma_1^-)\right)}, \end{aligned} \tag{22}$$

where $\tau(p, y^\infty, \Sigma^+)$ is the optical depth on the corresponding branch of the EFS. The notation here is the same as in Fig. 5: Σ^+ corresponds to the branch of the EFS that is located at $z > 0$. Accordingly, Σ_i^- is located at $z < 0$ and the subscript 1 corresponds to that branch that lies closer to the observer.

Relativistic effects may be important when calculating the escape/penetration probabilities and the source function. However, the Sobolev approximation makes all radiation transfer purely local. How quickly a photon is leaving the resonance is completely controlled and incorporated into the optical depth. The major difference from the non-relativistic case results from the aberration effects. That is, the radiation field emitted isotropically by the core is not seen as isotropic in the frame of the fluid. In the fluid frame the emission is assumed to be isotropic. Thus, in this frame, the expression of the source function, S will have the same look (in terms of penetration/escape probabilities) as in non-relativistic case. In the relativistic case, the derivation of this probability and also of the source function is given by Hutsemekers & Surdej (1995).

Having already calculated the optical depth (expression 8) we use the arguments of Hutsemekers & Surdej (1995) to derive the probability of a photon emitted in a line transition to escape in any direction from a given point in the envelope. To the order of v^2/c^2 it is expressed in the form

$$\beta_{\rm esc} = \frac{1}{4\pi}\int_{4\pi} \beta_{\rm loc}^{\mu}[1 + \beta^2(3\mu^2 - 1) + 2\mu\beta]\,{\rm d}\Omega, \tag{23}$$

where $\beta_{\rm loc}^{\mu}$ denotes the escape probability in the direction μ:

$$\beta_{\rm loc}^{\mu} = \frac{\{1 - \exp[-\tau_0(\mu, s)]\}}{\tau_0(s, \mu)}, \tag{24}$$

where τ_0 is given by (8). The penetration probability in the frame of the Sobolev approximation reduces to

$$\beta_{\rm pen} = \frac{1}{2}\int_{\mu_c}^{1} \beta_{\rm loc}^{\mu}\,{\rm d}\mu, \tag{25}$$

where $\mu_c = \cos\theta_c$, so that $\theta_c = \arccos\sqrt{1 - (1/x^2)}$ is the maximum angle at which the core is seen from the point x.

Weighting the intensity by the probability of a photon to penetrate to a given point, we obtain the mean intensity, J:

$$J = \frac{1}{4\pi}\int_{4\pi W} \beta_{\rm loc}^{\mu}(\theta, \phi) I_c\,{\rm d}\Omega, \tag{26}$$

with $\beta_{\rm loc}^{\mu}$ being defined by (24) and W a dilution factor:

$$W = \frac{1}{2}(1 - \mu_c). \tag{27}$$

The source function in the case of pure line scattering in the lab frame reads

$$S = \frac{J}{\beta_{\rm esc}}[1 + \beta^2(3\mu^2 - 1) + 2\mu\beta], \tag{28}$$

where $\beta_{\rm esc}$ should be found from (23) and terms of order v^2/c^2 were retained in (28). In the lab frame the source function (28) is clearly anisotropic, taking higher values in the direction of motion. For a relativistic formula see Hutsemekers & Surdej (1995), and for a non-relativistic see for example Mihalas (1978) and Castor (1970). A considerable simplification is obtained in the case of a linear velocity law $v(r) \sim r$, when, from (28) and (26), in the non-relativistic case one finds

$$S_{\rm lin} = I_c\frac{\beta_{\rm pen}}{\beta_{\rm esc}}, \qquad \text{where} \quad \frac{\beta_{\rm pen}}{\beta_{\rm esc}} = W. \tag{29}$$

Note that formulae (29) are applicable only in the case of a linear velocity law and when $\Phi \equiv 0$ at (8) so that $\beta_{\rm loc}^{\mu}$ does not depend on μ. In the case of an arbitrary velocity law or/and if the gravitational redshifting is taken into account, the integral in (26) must be evaluated in its general form.

Here we again emphasize our approximation in which we ignore the influence of the additional branches of the EFS on the mean intensity, J. That is, we ignore both negative $\sim e^{-\tau}$ and positive $\sim S(1 - e^{-\tau})$ contributions that may arise from resonant points on the line to the point where J is calculated.

After the intensity $I^\infty(y^\infty, p)$ has been calculated from (22), the normalized flux that is registered by the observer at infinity equals

$$F(y^\infty, p)/F_c = \int_0^{R_t} I^\infty(y^\infty, p) p\,{\rm d}p, \tag{30}$$

where F_c is the flux emitted by the core.

When calculating the redshifted absorption features, it has been found that the line profile at some frequencies displays notable oscillations. These oscillations are unphysical and arise from the specific behaviour of the source function on Σ^+ (see Fig. 5). The same effect has been found by Marti & Noerdlinger (1977) for a decelerating wind from a normal star. We find that the amplitude of these oscillations is reduced (very slowly in our calculations) when taking more points p_i. This is in fact a numerical artefact, which is related to the fact that the brightness of Σ^+ strongly depends on p when p approaches its maximum value $p_1 = \max(p \text{ on } \Sigma^+)$.

Thus, prior to calculation of the integral (30) we calculate p_1, the intersection of Σ^+ with the $z = 0$ plane. Then we split (30) into

$$\int_0^{p_1} I^\infty p \, \mathrm{d}p + \int_{p_1}^{p_{\rm out}} I^\infty p \, \mathrm{d}p.$$

This procedure allows us to eliminate completely spurious jumps of S on the boundary of Σ^+. It can also be useful in the calculations of decelerating winds from normal stars where there are EFS with sharp boundaries.

5 CALCULATION OF LINE PROFILES

Before we proceed to closer examination of line profiles, we need to make several assumptions about physical conditions existing in the flow. It is assumed that a spherically symmetric wind originates at the photosphere, which emits radiation in continuum. The radius of the photosphere is R^*. The radiation emitted by the core is resonantly absorbed (scattered) in a line of rest frequency ν_0 in the moving plasma. The relative importance of gravitational and Doppler red- and blueshifting is controlled by parameters R^* (i.e. $g_0 = R^*/r_{\rm g}$) and V^∞, respectively. Additionally, we specify the distribution of the opacity. Following the recipe of Castor & Lamers (1979), we parametrize the radial optical depth $\tau_{\rm r} = t(\mu = 1)$ (cf. equation 7), as a function of the velocity. The following dependences are considered:

$$\tau_{\rm r}(w) = T_0(k+1)\frac{(1-w)^k}{(1-w_{\rm c})} \tag{31}$$

and

$$\tau_{\rm r}(w) = T_0(k+1)\frac{w^k}{(1-w_{\rm c}^{k+1})}, \tag{32}$$

where $w \equiv v/V^\infty$ is the non-dimensional velocity, $w_{\rm c} = v(R^*)/V^\infty = 0.01$ and k is a free parameter. The parameter T_0 is related to the total optical depth at the line centre.

We adopt the following velocity laws: the linear velocity law (19), and the 'stellar' type velocity law:

$$w = w_{\rm c} + (1-w_{\rm c})\left(1 - \frac{1}{x^{\alpha_1}}\right)^{\alpha_2}, \tag{33}$$

where α_1, α_2 determine the slope and shape of the velocity profile. The velocity and opacity distributions for different pairs of α_1 and α_2, and for $k = 2$ and $k = -2$, are shown in Fig. 6.

For a given $g_0 = R^*/r_{\rm g}$, we specify y^∞ and calculate $v(r)$ from (19) or (33), and then calculate equal frequency surfaces from (18), then calculate $\tau_{\rm r}$ from (31), (32), and the source function from (28), and then the spectrum from (30).

Given the complex shape of the EFS, i.e. depending which branch of the EFS is tracked when looking for the roots of the equation (18), we switch between p, z or r, μ as independent variables. Additionally, in all calculations presented in this paper the occultation by the core is taken into account. Other parameters of the model are $v_{\rm th} = 5.7 \times 10^6\,{\rm cm\,s^{-1}}$, $R_{\rm t} = 100\,R^*$. The results are shown in Figs 7–11 and we consider them in turn.

5.1 $v \sim r$ law

In Section 3 it has been established that in the case of linear velocity law (19), the EFS (the redshifted part) may have two disconnected branches if the influence of strong gravity is taken into account and provided parameter g_0 is small enough (cf. Fig. 2). This is easily understood from the following arguments: in a normal stellar wind, $g_0 = R^*/r_{\rm g} \to \infty$, and the absorption feature may be formed only in that part of the wind that is approaching the observer, and thus is observed as blueshifted. In the case of a static configuration ($v = 0$) the EFS has the shape of a sphere of radius $x = |\zeta/2g_0y^\infty|$. A segment of this sphere which is projected on the core forms the *redshifted* absorption line. Redshifted photons could come from both the receding part of the wind, which is behind the core, and that

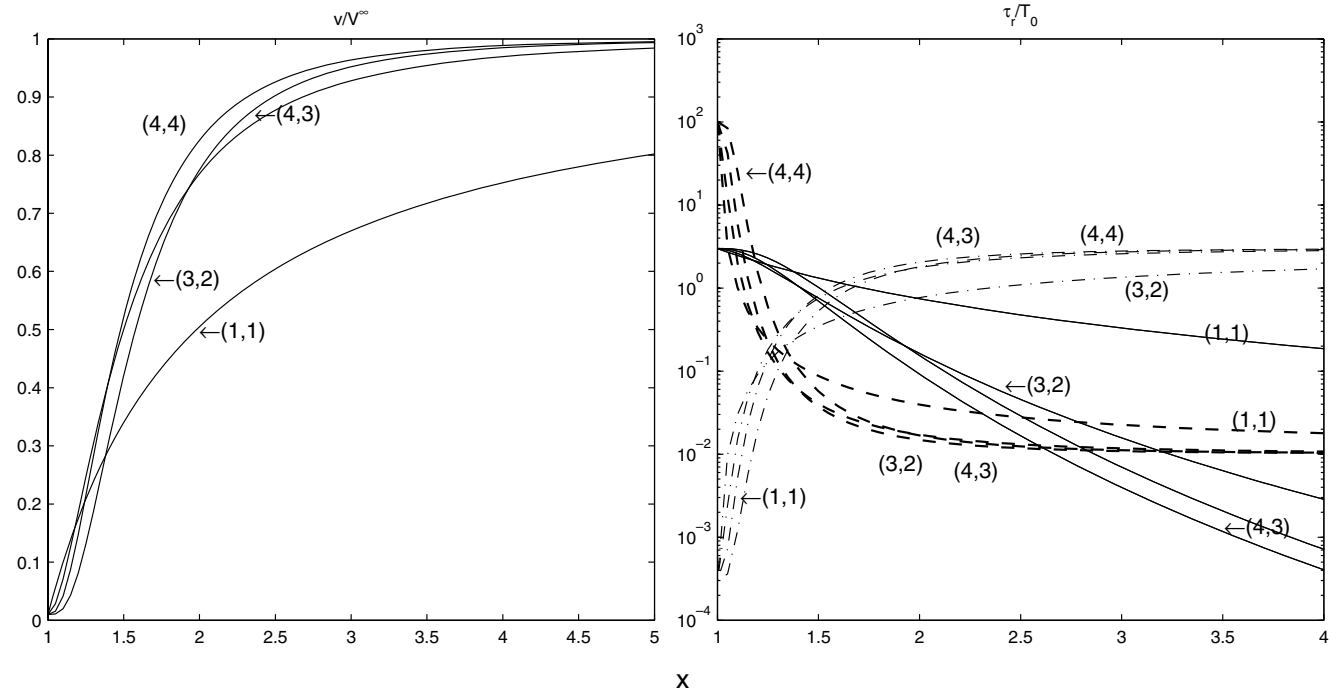

Figure 6. Velocity (left) and opacity (right) laws. Velocity law (33) with $w_{\rm c} = 0.01$. Opacity curves: solid line, equation (31); dashed line, equation (32), $k = -2$; dot–dashed line, equation (32), $k = 2$. Curves are marked by pairs of α_1, α_2 from (33).

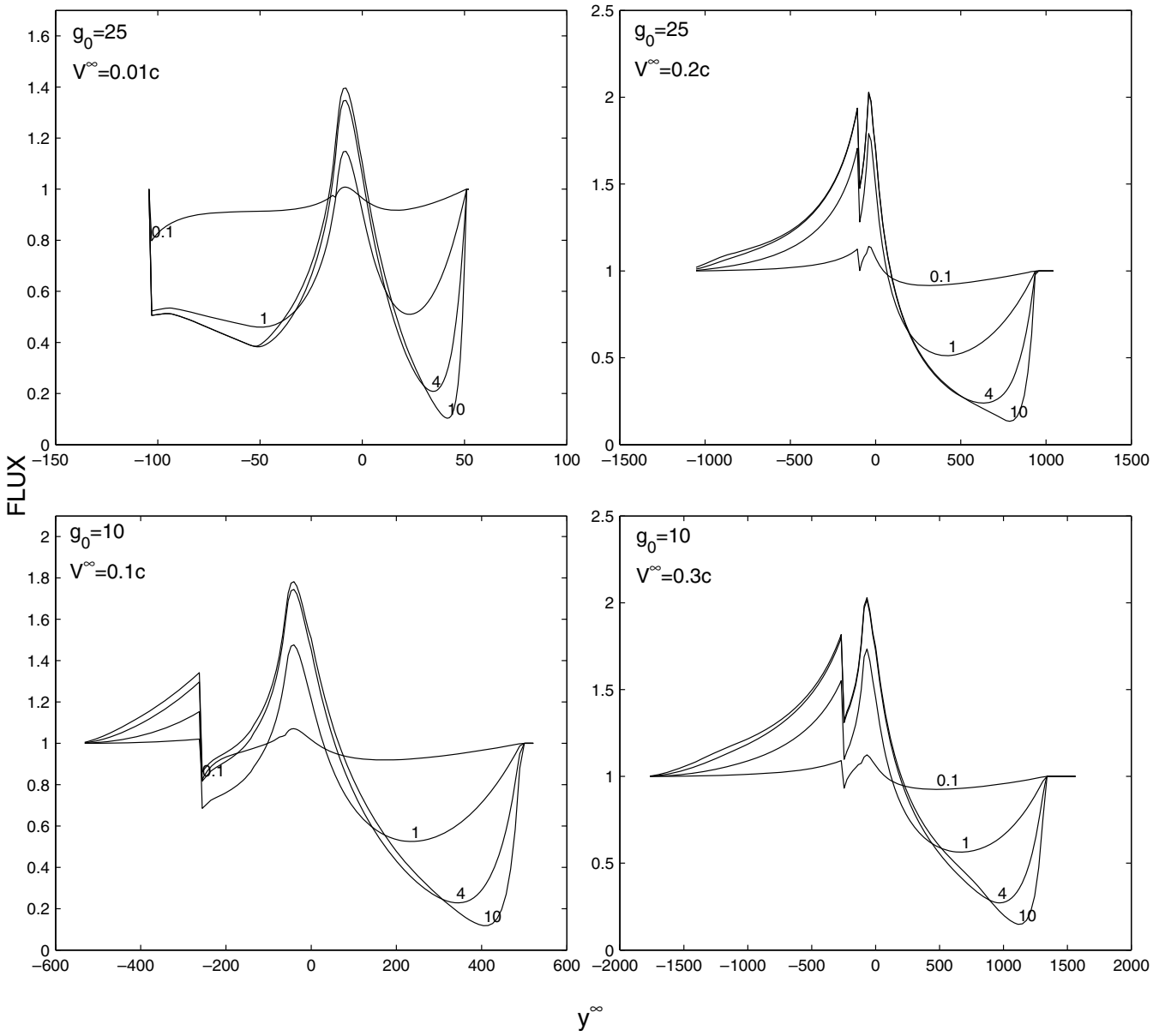

Figure 7. Profiles for $R^* = 25r_g$, $V^\infty = 0.01\ c$ (upper left), $R^* = 25r_g$, $V^\infty = 0.2\ c$ (upper right), $R^* = 10r_g$, $V^\infty = 0.1\ c$ (lower left), $R^* = 10r_g$, $V^\infty = 0.3\ c$ (lower right), and the linear velocity law (19). Curves are labelled by the total optical depth T_0. Notice the different vertical and horizontal scales in different panels. The left-hand plots have $V^\infty < V_{esc}$, where V_{esc} is the escape velocity at the wind launching point. Vertical axes denote flux. Horizontal axes denote frequency shift, y^∞.

branch of the EFS that is in front of it. In some cases, the re-emission from the receding gas may be faint since the source function is small: $S \sim r^{-2}$, and we may expect to observe a redshifted absorption feature. In such a case the resultant profile will be characterized by both blue- and redshifted absorption features.

Fig. 7 shows profiles for different terminal velocities and different launching radii. The strongest second absorption is observed for the lowest terminal velocity $V^\infty = 0.01\ c$ (upper left). Consider it in more detail: the maximum width of the redshifted absorption is set by $-\ y_{max}$ and y_{min}; in the picture, these are $y_{max} = 52.2$ and $y_{min} = -104.4$. We can see that the width of the second absorption component is of gravitational origin. Parameter V^∞ determines the width and strength of the blueshifted emission component.

Profiles for larger terminal velocity $V^\infty = (0.1 - 0.3)\ c$ and different g_0 show that for larger V^∞, and for a given $y^\infty < 0$, the EFS is located closer to the core and scatters more radiation, smearing the redshifted absorption line. A peculiar characteristic of these profiles is a redshifted absorption line superimposed on the background of the redshifted emission component. For example, if $g_0 = 10$, $V^\infty = 0.1c$, (lower left), the redward edge of the emission is set by $-\ y_{max} = -522$ and the redward edge of the redshifted absorption by $y_{min} = -261$.

In Fig. 8 the effect of different distributions of the opacity is shown. For $\tau_r \sim (1 - w)^k$ (left), resultant profiles are generally similar to those of $k = 2$ and $\tau_r \sim w^k$ (right). However, in other cases the results are quite distinct for different k.

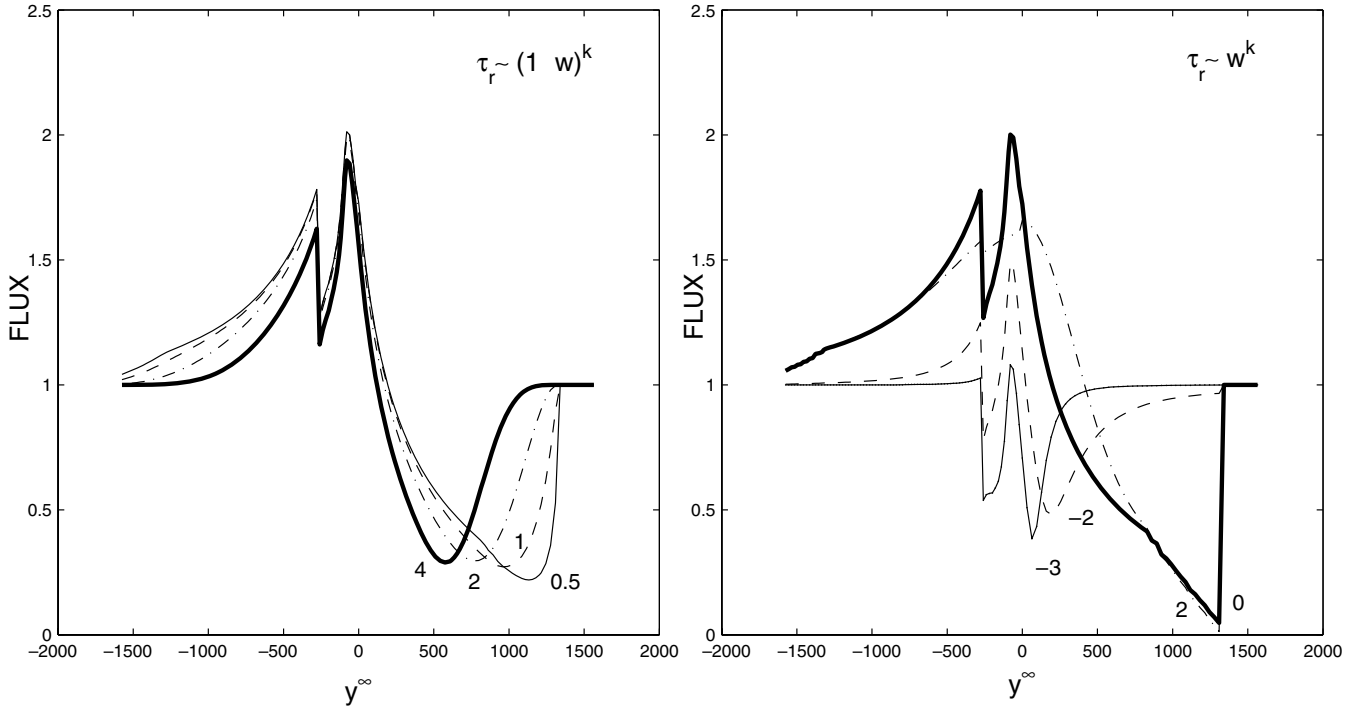

Figure 8. The effect of the distribution of different absorption laws: $\tau_r \sim (1-w)^k$ (left) and $\tau_r \sim w^k$ (right). Profiles for $R^* = 10r_g$, $V^\infty = 0.3\ c$ and $T_0 = 4$ and the linear velocity law (19). Curves are labelled by the parameter k. Vertical axes denote flux. Horizontal axes denote frequency shift, y^∞.

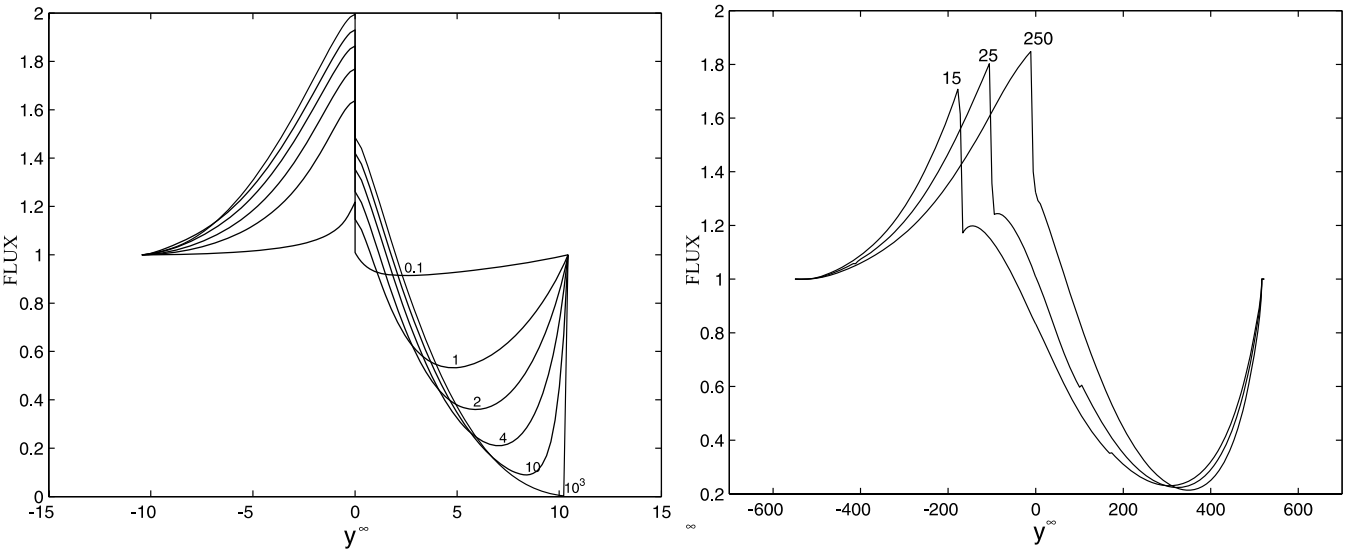

Figure 9. Profiles for $v(r) = V^\infty\ (1 - R^*/r)$. On the left the wind is launched at $R^* = 25 \times 10^3\ r_g$, having $V^\infty = 1897\,\mathrm{km\,s^{-1}}$. Each curve on this panel is labelled by the total optical depth, T_0. On the right the wind has $V^\infty = 0.1\ c$ and $T_0 = 4$, and curves are labelled by the parameter $g_0 = R^*/r_g$. In all cases the optical depth $t \sim (1 - w)$.

5.2 More realistic $v(r)$

First we calculate line profiles for parameters of the flow relevant to those for a wind from a normal star. These provide a good test of our results against those of Castor & Lamers (1979). Results are shown in Fig. 9. They are calculated for different values of T_0. The terminal velocity is $V^\infty \simeq 1897\,\mathrm{km\,s^{-1}}$.

The parameter $g_0 = 25 \times 10^3$ is taken large enough to ensure that gravitational redshifting is completely negligible in this case. Thus one expects to see no deviation of the resultant profiles from those of P Cygni. The profiles shown in Fig. 9 are in good agreement with those presented in fig. 7 of Castor & Lamers (1979) (note, however, that these authors use v/V^∞ as a frequency variable). In this case, the wind approaches the terminal velocity much more quickly than in the previous two cases. Profiles for the velocity law (20) are shown in Fig. (9) (right) for $T_0 = 4$. The increasing influence of the gravitational redshifting (decrease of g_0) results in shifting of the edge between the emission and absorption components to the

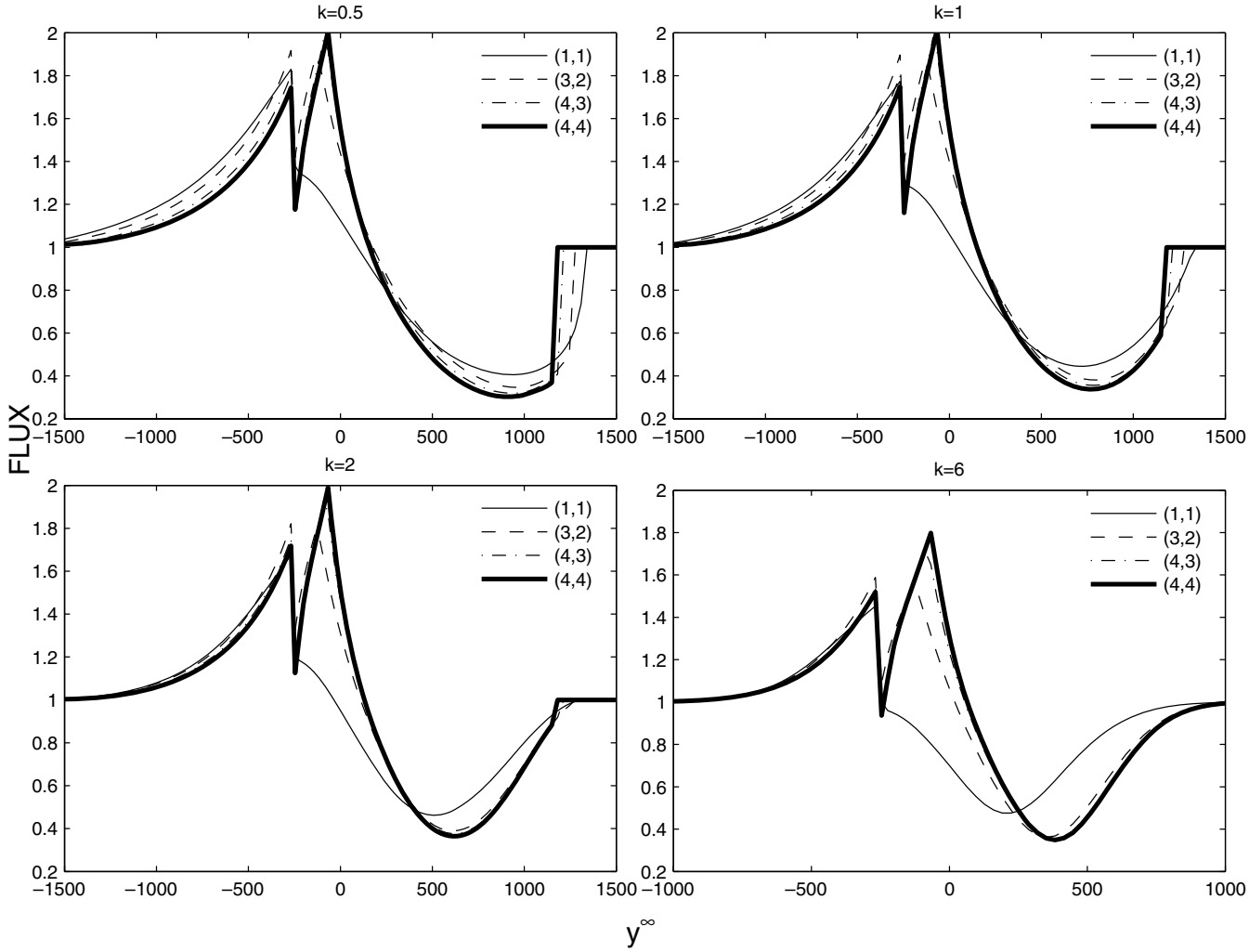

Figure 10. Profiles for $R^* = 10r_g, V^\infty = 0.3\ c, T_0 = 3$ using the velocity law (33) and $\tau \sim (1-w)^k$. Curves are labelled by pairs of parameters α_1, α_2.

left (to larger redshifts). For example, at $g_0 = 15$, the position of the edge $y^\infty \simeq -155$ is roughly determined by the Σ^+ component of the EFS (cf. Fig. 3 at $y^\infty = 0.8$, $y_{\min} = 140$). An interpretation is that the redshifted absorption almost exactly compensates for the redshifted emission. Increasing g_0 from 15 to 250 results in a shifting of this edge to the right, finally producing a line profile of the type shown in Fig. 9 (left).

As in the case of a linear velocity law, different distributions of opacity can significantly change the results (e.g. Castor 1970). The opacity is modified by varying the parameter k in (31) and (32). Additionally, parameters α_1 and α_2 can also be varied if using a general form of the velocity law (33).

A set of profiles for $\tau \sim (1-w)^k$ is shown in Fig. 10. The profiles are calculated for $R^* = 10r_g, V^\infty = 0.3\ c$ and $T_0 = 3$. Each panel shows them for different pairs of α_1, α_2 for the particular value of k. Again for $\alpha_{1,2} \neq 1$ a narrow absorption line is superimposed on the broad blueshifted emission line. Notice that in Fig. 10 the slowly accelerating wind ($\alpha_{1,2} = 1$) shows more absorption than in other cases of steeper accelerated winds. The centre of gravity of the emission peak in this case is dominated by photons coming from EFS that are located quite far away, behind the core (the wind is accelerating too slowly). These surfaces reflect too few photons ($S \sim 1/r^2$) and as a result the gravitationally redshifted absorption line dominates over the redshifted emission.

Fig. 11 shows the results for the same set of parameters as before but now for $\tau \sim w^k$. We see that the results are considerably different from the previous case. Only for $\alpha_{1,2} = 1$ are there profiles that look like classical P Cygni profiles. In most cases, the narrow absorption is superimposed on the blueshifted emission. For $k = -3$ and $k = -2$, profiles look similar to those obtained from the linear law (cf. Fig. 7).

5.2.1 *Shielding by the disc*

Our method, as presented in this paper, does not allow us to consider the anisotropic radiation field of an accretion disc or some additional attenuation of the emission. However, we can gain some insight by considering a wind that is viewed face on (i.e. perpendicular to the disc plane) and accounting for the blocking of those photons that are coming from behind such a disc. Since a significant part of the emission profile is formed by these photons, we want to know what happens if this emission is reduced. Thus we attenuate those photons by a factor of $e^{-\tau_{sh}}$, where τ_{sh} is the attenuation optical depth. The

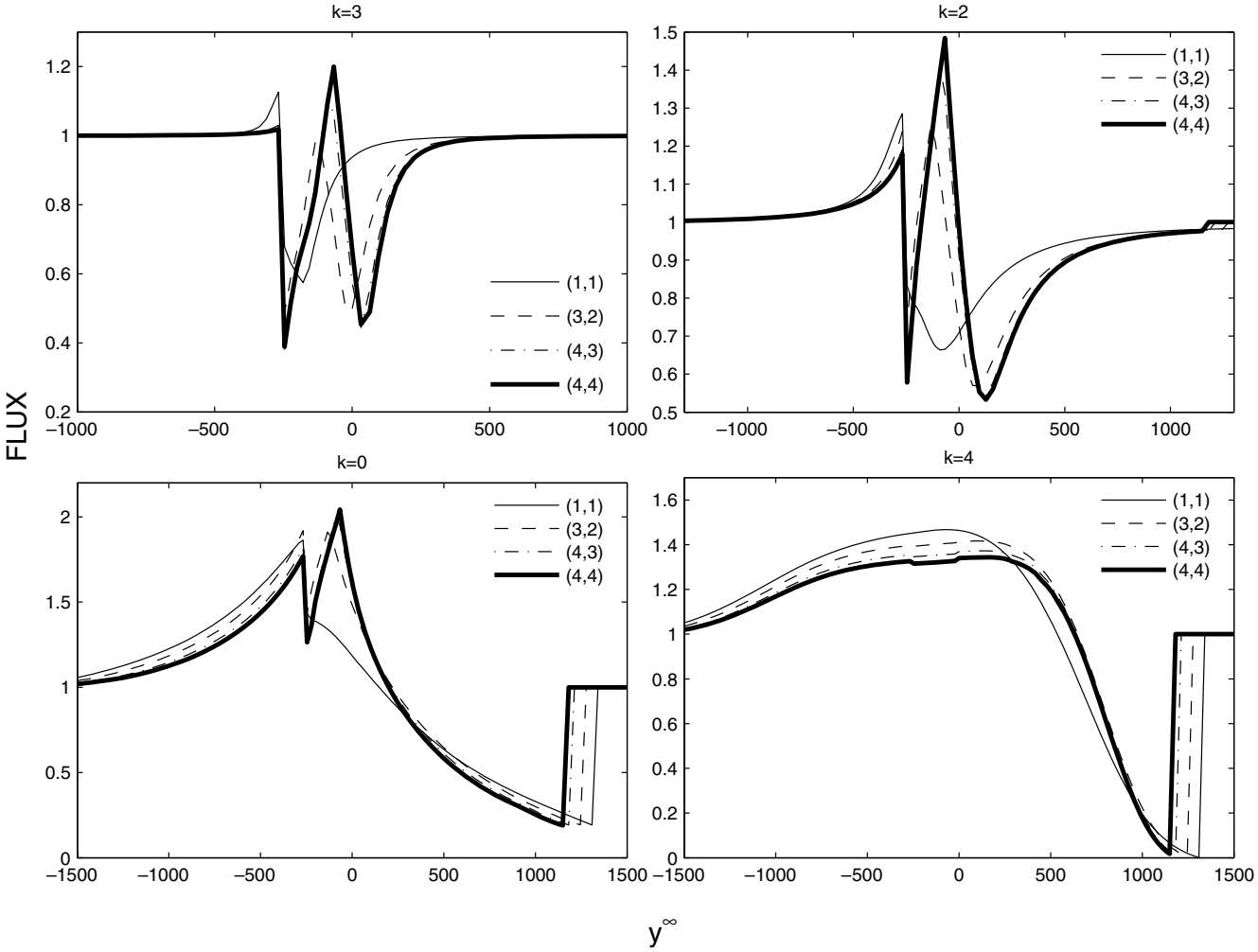

Figure 11. As Fig. 9; the parameter setup and labelling of the curves are the same. The opacity distribution is $\tau \sim w^k$.

results are shown in Fig. 12. As may be expected from the previous results, suppression of the emission leads to absorption–emission–absorption profiles regardless of the velocity law. That is because the emitting branches of the EFS, i.e. Σ_1^-, Σ_2^-, in Fig. 5 are screened but the absorptive branch Σ^+ is still there and absorbing radiation.

6 DISCUSSION

The strongest double absorption profile is found for the $v \sim r$ velocity law. The superposition of the gravitational redshift and Doppler shift easily produces two pronounced absorption features if the velocity law is not steep (as in the case of a linear law) or the maximum velocity within the line-forming region is small enough (as in Fig. 7, upper left). A more realistic velocity law (33) also gives W-shape profiles for several different values of α_1, α_2. In the case of a greater terminal velocity $v = 0.1$– $0.3\ c$ (i.e. of the order of the escape velocity at the base of the wind), in most cases the absorption feature is superimposed on the red emission wing of the line for both $\tau_r \sim (1-w)^k$ and $\tau_r \sim w^k$ distributions of the opacity. For the latter distribution, the W-shape profile is most pronounced, sometimes having approximately equal absorption troughs in the red and blue part of the spectrum (Fig. 11). Blocking of the emission (as in the case of an obscuring disc) also results in a W-shape profile (see Fig.12).

In order to produce an absorption feature, a certain resonant surface (or surfaces) must reside on the line of sight between the source of photons and an observer at infinity. In the case of the stellar (low gravity) wind and provided the velocity is gradually increasing, each EFS is single-valued. On the other hand, if the wind is decelerating then the EFS is not unique. If this is the case then photons emitted by one branch of the EFS can be scattered by the other and vice versa. As was shown above, the gravitational field introduces several new aspects, changing both the shape and the locus of EFS. The most important difference is the appearance of the resonant surface in front of the core and which is located in the *redward* part of the frequency domain. This component of the absorbing surface intersects the line of sight to the core and scatters any line radiation that crosses it. While multi-branched EFS are not new, the appearance of the surface of equal redshift in front of the core for outwardly accelerated flow is not known in the theory of stellar winds.

This may be made clear if we imagine a static and extended distribution of plasma around a compact object. In this imaginary exercise, it is only gravitational redshifting that is important and the corresponding EFS is just a sphere that is concentric with the centre of gravity.

In a moving plasma this spherical EFS is transformed depending on the velocity law, such that for certain redshifts there is a

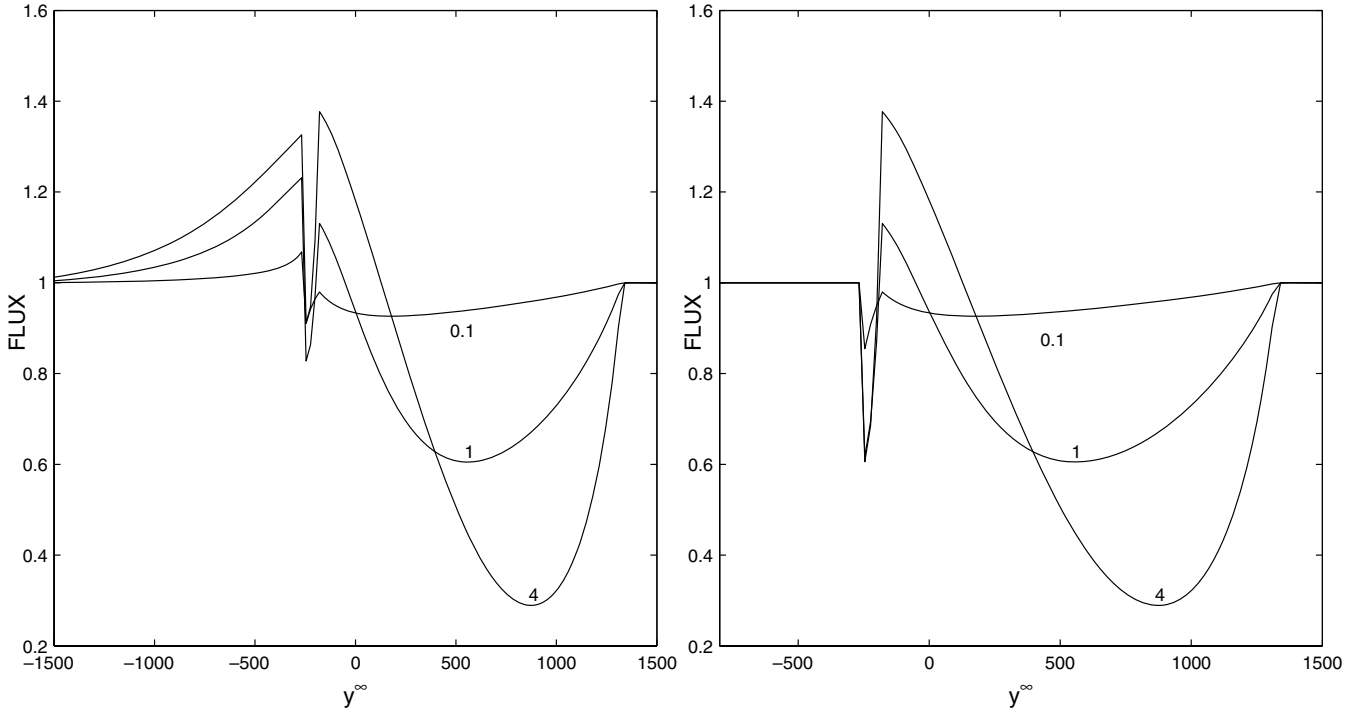

Figure 12. The effect of shielding of the emission component. Curves are calculated for $\tau \sim (1 - w)$: left, $\tau_{\rm sh} = 1$; right, $\tau_{\rm sh} = 10$. Labelling: total optical depth T_0. Other parameters: $R^* = 10r_{\rm g}$, $V^\infty = 0.3c$.

component in front of the the core (cf. Fig. 2). Absorption within this EFS may form an absorption feature in the redshifted part of the line profile.

The emission component is formed in the same way as in the stellar case, namely because of the large surface area of those EFS that are not intersecting the line of sight between the observer and the core. This redshifted emission is superimposed on the absorption line. The net result depends on the distribution of the opacity, i.e. on the amount of scattered radiation. The blueshifted part of the profile is formed because of the interaction of the *blue* continuum photons with resonant EFS giving the absorption feature for the blue part of the profile. The value of V^∞ roughly sets the width of the redshifted emission and blueshifted absorption. Results show that the centroid energy of the blueshifted absorption depends on the distribution of the opacity, and can be seen at significantly smaller shifts. If the gravitational redshift effect is significant but smaller than the pure Doppler effect, there exists some maximum redshift at which the EFS has a component at $z > 0$. This component attenuates the core radiation as $I_{\rm c}{\rm e}^{-\tau(\Sigma^+)}$ (22), and produces an absorption feature superimposed on the emission component, as in Figs 10–12. Here, again, the details depend sensitively on the distribution of the opacity.

The intensity $I(y^\infty, p)$ is composed of the radiation of the core, $\sim I_{\rm c}\,{\rm e}^{-\tau}$, and the contribution

$$\oint_{\Sigma_i} S(x, y)(1 - {\rm e}^{-\tau_{\Sigma_i}})\,{\rm d}x\,{\rm d}y,$$

where the integral is carried along the resonant surface. In the case of pure line scattering $S \sim 1/r^2$, and the 'brightness' of the emission line is determined by the surface area of the resonant surface, balanced by the $1/r^2$ divergence of the radiation flux. Thus, it is not enough to have opacity concentrated at smaller, or larger r. If at small r the absorption and gravitational field are strong, the absorption feature may be strong but the redshifted emission formed by scattered radiation is also strong. In the other extreme, at large r the emission may be very faint because of the small flux. The shape of the EFS is also important. Without actual calculation of the EFS there is no way to tell which is stronger, the redshifted emission or redshifted absorption.

The conclusion is that if absorption takes place in a spectral line within a wind, provided that the plasma is moving radially and gradually accelerated in strong gravity then a profile with two absorption features is quite possible; in some cases there is a prominent emission component, and the profile is observed as W-shaped.

The results are sensitive to the assumptions about the opacity and velocity; the geometry of the EFS depends on the distribution of $v(r)$ and on $g_0 = R^*/r_{\rm g}$; the amount of scattered radiation depends on the distribution of the opacity. If it is concentrated towards the star (as in Fig. 6), the conditions favour the formation of a W-shaped profile. However in each case different possibilities in choosing $v(r)$ and $\tau_{\rm r}(r)$ should be considered.

7 CONCLUSIONS

Our goal in this paper has been to study shapes of spectral lines from a plasma that is rapidly moving in the vicinity of a neutron star or a black hole. The latter case can account for both stellar (Galactic black hole candidates) and supermassive BHs (AGN). In the well-studied case of winds from normal hot stars, a rapidly moving wind interacts with the continuum radiation of a star and produces a P Cygni profile. From the theory of stellar winds it is known that in the case of an arbitrary spherically symmetrical distribution of plasma that is moving with a gradually increasing velocity, an absorption line that is blueshifted with respect to the emission line is observed. This is widely interpreted as a fingerprint of moving plasma in a variety of astrophysical situations.

In this paper, shapes of line profiles for several velocity and opacity distributions were calculated taking into account gravitational redshifting.

Strong gravitational redshifting helps the radiation to escape efficiently and to interact with matter only locally. This has already been established to be dynamically important. The papers by Dorodnitsyn (2003) and Dorodnitsyn & Novikov (2005) addressed the problem of plasma acceleration driven by radiation pressure in spectral lines, provided that the flow is launched in the vicinity of a compact object. It was shown that it is important to include gravitational redshifting in the calculations of the radiation force. The radiation pressure depends on $\mathrm{d}\phi/\mathrm{d}r$ and $\mathrm{d}v/\mathrm{d}r$, while in the case of an O-type star wind it depends only on $\mathrm{d}v/\mathrm{d}r$. Proximity to a compact object, i.e. strong ionizing radiation, makes it difficult for heavy ions to survive without being completely stripped of electrons, so the efficiency of this additional mechanism in real situations depends on the simultaneous solution for the ionization balance and accounting for other possible mechanisms (such as clumping) that prevent over-ionization of the flow.

We are also motivated by the current accumulating evidence for gravitationally redshifted narrow absorption features in many AGN spectra as well as by observations of gravitationally redshifted absorption lines in the X-ray burst spectra of neutron stars. A potentially interesting example of the latter is presented by the observations of the gravitationally redshifted absorption lines in the X-ray burst spectra of EXO0748−676 (Cottam et al. 2002). If the interpretation is correct, these features are produced close to the compact object, where extreme conditions are coupled with high-amplitude fluctuations of the radiation field and short dynamical time-scale. As a result, these lines may be highly variable or/and transient. The non-detection of gravitationally redshifted lines in the observations of the other suitable-looking candidate GS, 1826−24 (Kong et al. 2007) may be an example.

Given the diverse nature of these objects, it is desirable to consider a model with a minimum number of free parameters and in so doing we assume our outflow to be spherically symmetric and exposed to the continuum radiation of a spherical core.

Realistic models should consider the departure of the outflow and the radiation field from spherical symmetry. Bending of the photon trajectories in the strong gravitational field of the compact object may play some role. In our calculations we did not take this into account because we were concerned with regions of the flow located approximately at radii $>10r_{\mathrm{g}}$.

In our calculations the idea of equal frequency surfaces (EFS) plays a major role. The strong gravitational field changes the shape and locus of such surfaces. Their topology is complex; the gravitational field strongly distorts the P Cygni profile. Some branches of the EFS in the *redshifted* part of the spectra are found to be in front of the core, meaning there is the possibility for the absorption component to be observed as *redshifted* with respect to the emission.

From numerical calculations, which are second-order accurate in v/c, it is established that a superposition of Doppler and gravitational shifting of frequency can distort the P Cygni profile in such a way that blue- and redshifted absorption features are observed simultaneously. Often the redshifted absorption line is superimposed on the emission wing. This effect is, of course, strongest close to the compact object. However, the emission part is also stronger there, and it may smear the absorption trough. Necessarily, the second absorption arises if the velocity profile is not very steep and at the same time the line-forming region is situated within several tens of r_{g}. However the former requirement is not crucial, if the line opacity peaks close to the compact object. Profiles with more than one emission and two absorption features are possible. However, in a model of pure line scattering, those additional (i.e supplementary to W-shape profile) features would be considerably weaker.

Different modifications of 'stellar' type velocity laws were adopted. Such velocity profiles describe stationary spherically symmetric hydrodynamical flows. A well-known example of such is the $v \sim \sqrt{1-1/x}$ profile. Note that different modifications of this law were obtained by different authors using both theoretical and observational arguments (see e.g. Castor & Lamers 1979). Thus we adopted a generalized form of this law, $v \sim (1-1/x^{\alpha_1})^{\alpha_2}$. In the case of non-magnetic accretion disc winds, the azimuthal component of the velocity quickly becomes much smaller than the radial one, and such a velocity profile describes the real distribution of the line-of-sight velocity reasonably well.

During X-ray bursts, the situation can be more complicated. During the burst, the temperature at the stellar photosphere may quickly approach $T \sim 10^9$ K and electron scattering occurs in the Klein–Nishina regime. The reduced cross-section allows for higher radiation flux (locally below Eddington) to diffuse out to larger radii, where the temperature is lower and the radiation flux is locally super-Eddington. A quasi-stationary wind may result. Calculations of such winds must self-consistently account for the radiation transfer and relativistic corrections and demonstrate stellar-type velocity profiles (Quinn & Paczynski 1984; Nobili, Turolla & Lapidus 1994.)

To approximate the explosively accelerated plasma of X-ray bursters we adopt a linear velocity law. Making use of a Hubble law, $\boldsymbol{v} = \boldsymbol{r}/t$ drastically simplifies the radiation transfer calculations in supernova shells (Karp et al. 1977).

Two parametrized opacity laws and a linear, and generalized, form of the velocity law, $v \sim (1-1/x^{\alpha_1})^{\alpha_2}$ were considered.

Our results for all considered velocity and opacity distributions show that in particular circumstances, i.e. proper velocity and opacity laws and strong gravity, the observed line profile consists of two absorption troughs separated by the emission component. The redshifted absorption line can be weak and can be superimposed on the emission wing. Some of the strongest W-shape profiles were found for the linear velocity law. Surprisingly enough, no W-shape profiles are found for a $v \sim \sqrt{1-1/x}$ law. In this case the redshifted absorption almost exactly compensates for the blueward emission peak, producing a sharp edge in the emission (Fig. 9).

However, in many other cases of different α_1, α_2, W-shape profiles are also found (Figs 10–11). If the opacity is distributed as $\tau \sim (1-v/V^{\infty})^k$, $(k>0)$, the redshifted absorption line in most cases is superimposed on the redshifted emission. However, if the opacity peaks at smaller velocities, $\tau \sim 1/v^k$, distinct W-shape profiles are found again. Thus, the results suggest that the most favourable conditions are realized when the opacity peaks at large gravitational redshifts, and in such a case the velocity profile is probably less important. The further the distribution of the opacity is from that, the more important is the velocity law and the relative importance of the Doppler effect.

If some observed spectral feature is interpreted as being formed in the flow in a proximity of a strongly gravitating compact object, then our results suggest that the assumption of the distribution of the opacity (optical depth law) is the most critical one. Such a distribution should be calculated simultaneously with the ionization balance calculations in the background of the pre-calculated hydrodynamical model.

The separation between red- and blueshifted absorption features is a function only of the dynamics and relative importance of gravity in the line-forming region.

The most robust prediction of our model is the possibility of the double absorption trough resulting from a concurrence between gravitational redshifting and Doppler effects. Our calculations suggest that the particular shape and intensity of the emission component that separates these absorption lines depends sensitively on assumed parameters.

Gravitationally redshifted absorption lines form in places close to the compact object. The emission component is necessarily formed in plasma occupying a much larger volume. Thus, these features are formed in places that are possibly strongly separated in space. From the perspective of future observations, it would be interesting to look for correlated variability of different components of the profile between each other and with the continuum.

ACKNOWLEDGMENTS

Most of this work was carried out when the author was a postdoctoral fellow at the Max Planck Institute for Nuclear Research (Heidelberg). This research was supported in part by an appointment to the NASA Postdoctoral Program at the NASA Goddard Space Flight Center, administered by Oak Ridge Associated Universities through a contract with NASA. The author thanks G.S. Bisnovatyi-Kogan for the encouragement of this work and also Felix Aharonian and members of the High Energy Astrophysics Group of the Max Planck Institute for Nuclear Research for discussion. The author thanks Tim Kallman for discussions and his suggestions and help regarding the style and structure of the manuscript.

REFERENCES

Beals C. S., 1931, MNRAS, 91, 966B
Blandford R. D., Payne D. G., 1982, MNRAS, 199, 883
Castor J. I., 1970, MNRAS, 149, 111
Castor J. I., Lamers H. J. G. L. M., 1979, ApJ, 39, 481
Cottam J., Paerels F., Mendez M., 2002, Nat, 420, 51
Dadina M., Cappi M., Malaguti G., Ponti G., de Rosa A., 2005, A&A, 442, 461
Dorodnitsyn A. V., 2003, MNRAS, 339, 569
Dorodnitsyn A. V., Novikov I. D., 2005, ApJ, 621, 932
Fabian A. C., Iwasawa K., Reynolds C. S., Yong A. J., 2000, PASP, 112, 1145
Grachev S. I., Grinin V. P., 1975, Astrophys., 11, 20
Hutsemekers D., Surdej J., 1990, ApJ, 361, 367
Jeffery D. J., 1995, ApJ, 440, 810
Karp A. H., Lasher G., Chan K. L., Salpeter E. E., 1977, ApJ, 214, 161
Kong A. et al., 2007, ApJ, 670, L17
Kuan P., Kuhi L. V., 1975, ApJ, 199, 148
Landau L. D., Lifshitz E. M., 1960, The Classical Theory of Fields. Pergamon, New York
Marti F., Noerdlinger P. D., 1977, ApJ, 215, 247
Matt G., Porquet D., Bianchi S., Falocco S., Maiolino R., Reeves J. N., Zappacosta L., 2005, A&A, 435, 857
Mihalas D., 1978, Stellar Atmospheres. Freeman, San Francisco
Morton D. C., 1967, ApJ, 150, 535
Nandra K., George I. M., Mushotzky R. F., Turner T. J., Yaqoob T., 1999, ApJ, 523, 17
Nobili L., Turolla R., Lapidus I., 1994, ApJ, 433, 276
Paczynski B., Wiita P. J., 1980, A&A, 88, 23
Quinn T., Paczynski B., 1984, ApJ, 289, 634
Reeves J. N., Pounds K., Uttley P., Kraemer S., Mushotzky R., Yaqoob T., George I. M., Turner T. J., 2005, ApJ, 633, L81
Rybicki G. B., Hummer D. G., 1978, ApJ, 219, 654
Sobolev V. V., 1960, Moving envelopes of stars. Harvard Univ. Press, Cambridge MA
Surdej J., 1977, A&A, 60, 303
Yaqoob T., Padmanabhan U., 2005, ApJ, 604, 63
Yaqoob T., Serlemitsos P., 2005, ApJ, 623, 112

This paper has been typeset from a TEX/LATEX file prepared by the author.